Structure
Article

Binding Mechanism of Metal·NTP Substrates and Stringent-Response Alarmones to Bacterial DnaG-Type Primases

Richard U. Rymer,[1] Francisco A. Solorio,[2] Ashley K. Tehranchi,[3] Clement Chu,[4] Jacob E. Corn,[5] James L. Keck,[6] Jue D. Wang,[3] and James M. Berger[1,*]

[1]California Institute for Quantitative Biosciences, 374D Stanley Hall #3220, University of California, Berkeley, Berkeley, CA 94720-3220, USA
[2]1490 60th Avenue, Sacramento, CA 95822, USA
[3]Department of Molecular and Human Genetics, Baylor College of Medicine, One Baylor Plaza, MS BCM225, Houston, TX 77030, USA
[4]University of California, San Francisco, 600 16th Street, Box 2140, Genentech Hall S252B, San Francisco, CA 94143-2140, USA
[5]Department of Early Discovery Biochemistry, Genentech, 1 DNA Way, South San Francisco, CA 94080, USA
[6]Department of Biomolecular Chemistry, 420 Henry Mall, University of Wisconsin School of Medicine and Public Health, Madison, WI 53706, USA
*Correspondence: jmberger@berkeley.edu
http://dx.doi.org/10.1016/j.str.2012.05.017

SUMMARY

Primases are DNA-dependent RNA polymerases found in all cellular organisms. In bacteria, primer synthesis is carried out by DnaG, an essential enzyme that serves as a key component of DNA replication initiation, progression, and restart. How DnaG associates with nucleotide substrates and how certain naturally prevalent nucleotide analogs impair DnaG function are unknown. We have examined one of the earliest stages in primer synthesis and its control by solving crystal structures of the *S. aureus* DnaG catalytic core bound to metal ion cofactors and either individual nucleoside triphosphates or the nucleotidyl alarmones, pppGpp and ppGpp. These structures, together with both biochemical analyses and comparative studies of enzymes that use the same catalytic fold as DnaG, pinpoint the predominant nucleotide-binding site of DnaG and explain how the induction of the stringent response in bacteria interferes with primer synthesis.

INTRODUCTION

DNA replication is a highly choreographed and tightly regulated event in the life cycle of all cells (Kornberg and Tania, 1992). Carried out by a dynamic, multiprotein complex known as the replisome, the process of replication relies on the coordinated and coupled action of DNA unwinding with strand synthesis. Although many differences exist among bacterial, archaeal, and eukaryotic replisomes, they all utilize a specialized type of DNA-dependent RNA polymerase, termed primase, to synthesize short RNA oligonucleotides (Frick and Richardson, 2001). These RNA primers in turn serve as indispensable starting points for extension by DNA polymerases, which are incapable of initiating strand synthesis de novo (Frick and Richardson, 2001; Kuchta and Stengel, 2010).

In bacteria, a protein known as DnaG is responsible for catalyzing primer synthesis during DNA replication (Kitani et al., 1985; Rowen and Kornberg, 1978). DnaG was discovered through the identification of "fast-stop" mutations in the *dnaG* gene in early screens for temperature-sensitive replication defects (Carl, 1970). DnaG is now known to play a critical role in numerous replicative processes, including replisome assembly (Makowska-Grzyska and Kaguni, 2010), the control of fork progression (Chintakayala et al., 2009; Lee et al., 2006; Salzberg et al., 1998; Tanner et al., 2008), the regulation Okazaki fragment length (Wu et al., 1992a, 1992b; Zechner et al., 1992), and replication fork restart (Heller and Marians, 2006). Recent work has further shown that DnaG is a target for inhibiting DNA replication under conditions of nutrient deprivation (Maciag et al., 2010; Wang et al., 2007), a process known as the stringent response. Thus, primer synthesis and DnaG itself are central nodes for regulating replication in bacteria as whole.

Overall, three general strategies to controlling DnaG function have been identified. One relies on the selective recruitment of DnaG to a specific site of action. For example *Escherichia coli* DnaG interacts with both the replicative helicase, DnaB (Griep and Lokey, 1996; Marians, 1992; Tougu et al., 1994; Wu et al., 1992a), and the single-stranded DNA-binding protein, SSB (Sun and Godson, 1996; Sun et al., 1994), interactions that allow DnaG to interface with distinct replisomal processes (Heller and Marians, 2006; Tougu and Marians, 1996a). A second strategy involves the localized control of primer synthesis. Once bound to DnaB, DnaG can self-associate as a means to both determine the starting position for primer synthesis and control primer length (Bhattacharyya and Griep, 2000; Chintakayala et al., 2009; Corn et al., 2005; Hamdan and van Oijen, 2010; Tougu and Marians, 1996b; van Oijen and Loparo, 2010). The third approach is the use of noncanonical nucleotides, such as the stringent response effectors (p)ppGpp, which directly impede primer formation (Maciag et al., 2010; Swart and Griep, 1995; Wang et al., 2007). At present, how these various protein/protein and protein/ligand interactions influence the catalytic properties of DnaG is not understood.

Although comparative studies to other DNA- and RNA-synthesizing enzymes should in principle be useful for understanding

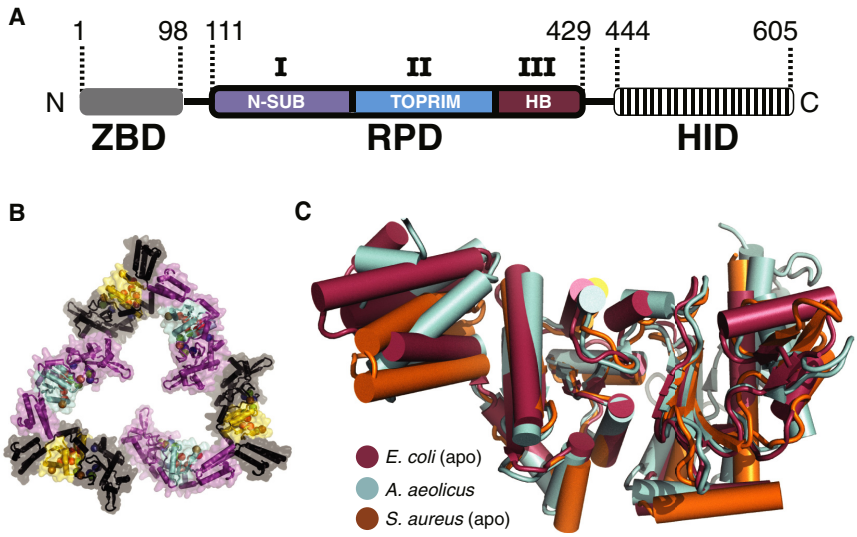

Figure 1. Structure of the *S. aureus* DnaG RPD

(A) Schematic of DnaG domain structure is illustrated. ZBD, zinc-binding domain; HID, helicase interaction domain. Subdomains of the RPD (Figure S1) are N-terminal subdomain (N-SUB) (I), TOPRIM fold (II), and helical bundle (HB) (III).

(B) The *S. aureus* DnaG RPD active site is solvent accessible. Cartoon and surface representation is shown for the crystal packing arrangement of *S. aureus* DnaG RPD protomers. Six protomers, related by crystal symmetry, are shown. Three are colored purple with cyan active sites; three are black with yellow active sites. Spheres denote the C_α positions of functionally important residues in the active site.

(C) Superposition of several DnaG RPDs solved to date. Structures, corresponding to known apo states, are shown as cartoons and colored as follows: *E. coli* RPD, maroon (PDB 1DDE); *A. aeolicus* RPD, cyan (PDB 2AU3); and *S. aureus* RPD, orange (PDB 4E2K).

these regulatory phenomena, DnaG is unusual among replicative polymerases in that it bears no evolutionary kinship to either the archaeal/eukaryl primase or any other polymerase lineage (Frick and Richardson, 2001; Kuchta and Stengel, 2010). Instead, the RNA-Polymerase Domain (RPD) of DnaG (Figure 1A) is related to the metal-binding center of type IA and type II topoisomerases, a region termed the TOPRIM (*TO*poisomerase/*PRIM*ase) domain (Aravind et al., 1998; Keck et al., 2000; Podobnik et al., 2000). Although several models have been proposed for how DnaG forms a productive ternary complex with template, NTPs, and/or a newly formed primer (Corn et al., 2008; Kato et al., 2003; Keck et al., 2000; Podobnik et al., 2000), only a single partial complex—one in which single-stranded DNA is bound (Corn et al., 2008)—currently exists. As a consequence, the mechanisms of substrate recognition and catalysis by DnaG are ill defined compared to other polymerases.

Barriers to conducting structural investigations of DnaG stem largely from its challenging biochemical properties. In particular, the enzyme has a relatively low affinity for substrates such as RNA•DNA heteroduplexes (~50 μM) (Mitkova et al., 2003), which has precluded the straightforward determination of pertinent cocrystal structures. However, DnaG-type primases are known to productively bind individual nucleotides in the midmicromolar range (Mendelman et al., 1994; Swart and Griep, 1995), a property that should in principle allow for the use of high NTP concentrations to drive complex formation. Here, we have taken advantage of this property to obtain several crystal structures of the *Staphylococcus aureus* DnaG RPD in complex with individual nucleotides and their metal-ion cofactors. These structures, together with biochemical studies and structural comparisons that validate these interactions, reveal an unexpected location and orientation for nucleotide binding within the TOPRIM region of the enzyme. The observed manner of binding in turn both highlights a mechanistic role for a number of conserved amino acids in the DnaG family and reconciles the disparate models of DnaG-substrate engagement present in the literature. Additional structures with the stringent response alarmones pppGpp (G5P) and ppGpp (G4P) further reveal an unanticipated binding modality for these agents that accounts for their mixed inhibitor-type behavior in disrupting primer synthesis.

RESULTS AND DISCUSSION

Structures of *S. aureus* DnaG RPD·NTP Complexes

Initial efforts to soak NTPs into crystals comprising the RPDs of either *E. coli* or *Aquifex aeolicus* DnaG were unsuccessful, likely due to tight packing environments that occluded their respective catalytic centers (Corn et al., 2005; Keck et al., 2000; Podobnik et al., 2000). To circumvent this problem, we surveyed the DnaG RPDs from several bacterial species for a more suitable crystal form. This investigation identified crystallization conditions for a previously uncharacterized RPD from *S. aureus* (*Sa*DnaG), which diffracted to 2 Å resolution and contained an arrangement of protomers with solvent-accessible active sites (Figure 1B). Molecular replacement (MR) was used to generate initial phases for these data, which allowed for the subsequent building and refinement of the structure (Experimental Procedures). The final model has an R_{work}/R_{free} of 19.1%/21.7%, with excellent geometry as judged by MolProbity (Table 1) (Chen et al., 2010). The *S. aureus* RPD superposes well with other RPDs solved to date, having an average C_α rmsd of ~1 Å (Figure 1C); only the relative orientation of a poorly conserved C-terminal helical bundle differs appreciably among the structures.

The *Sa*DnaG RPD crystallographic system facilitated the soaking of divalent metal ions and various NTPs to obtain nucleotide-bound complexes (Experimental Procedures). Manganese initially was chosen over magnesium for these studies because primase works equally well with either cofactor (Godson et al., 2000; Rodina and Godson, 2006), and because the spectral properties of manganese enabled the unambiguous determination of its presence from anomalous diffraction data. Crystals treated in this manner diffracted to a similar resolution as apo crystals, indicating that the soaking procedure did not induce crystal damage. Structures were determined for each of the four ribonucleotide substrates using MR and refined to a similar

Table 1. Data Collection and Refinement Statistics

	Apo *Sa*DnaG RPD 4E2K[a]	ATP-Bound *Sa*DnaG RPD 4EDG[a]	CTP-Bound *Sa*DnaG RPD 4EE1[a]	GTP-Bound *Sa*DnaG RPD 4EDK[a]	UTP-Bound *Sa*DnaG RPD 4EDR[a]	G5P-Bound *Sa*DnaG RPD 4EDV[a]	G4P-Bound *Sa*DnaG RPD 4EDT[a]
Crystal Data							
Space group	P 6_1	P 6_1	P 6_1	P 6_1	P 6_1	P 6_1	P 6_1
Cell dimensions (a, b, c [Å], α, β, γ [°])	151.3, 151.3, 38.5, 90, 90, 120	152.3, 152.3, 38.7, 90, 90, 120	152.2, 152.2, 38.8, 90, 90, 120	152.2, 152.2, 38.8, 90, 90, 120	150.6, 150.6, 38.6, 90, 90, 120	152.6, 152.6, 38.6, 90, 90, 120	150.2, 150.2, 38.6, 90, 90, 120
Data collection	Native	Native	Native	Native	Native	Native	Native
Wavelength (Å)	1.115	1.115	1.115	1.115	1.115	1.115	1.115
Resolution (Å)	50.00–2.15	34.59–2.00	30.62–1.99	49.6–2.00	37.04–2.01	38.64–2.01	43.4–2.00
Reflections (measured/unique)	248,259/28,064	187,094/34,499	368,265/32,369	506,322/35,005	183,488/33,847	277,309/34,211	284,153/35,073
R_{sym} (%) (highest shell)[b]	7.2 (64.7)	4.6 (28.7)	11.3 (68.2)	9.4 (49.5)	4.7 (17.3)	8.3 (57.2)	7.5 (63.0)
$\langle I/\sigma I \rangle$ (highest shell)	30.5 (3.9)	22.2 (5.2)	14.8 (4.1)	21.8 (5.3)	10.9 (3.6)	17.8 (4.1)	18.7 (3.2)
Completeness (%) (highest shell)	100 (100)	99.8 (98.8)	94.7 (100)	100 (100)	99.9 (100)	99.8 (99.8)	99.7 (98.1)
Redundancy	8.8	5.3	11.4	10.8	5.4	8.2	8.2
Refinement							
R_{work}/R_{free} (%)[c]	19.1/21.7	16.2/19.7	18.2/21.6	16.1/20.0	17.2/20.5	16.7/20.3	18.0/22.0
Average B factor (Å^2)							
Protein	39.4	34.8	26.9	32.3	28.8	36.4	39.4
Solvent	44.8	46.8	39.6	43.9	40.9	47.6	50.3
Rmsd							
Bond lengths (Å)	0.006	0.02	0.002	0.002	0.002	0.003	0.011
Bond angle (°)	0.77	0.715	0.637	0.681	0.735	0.705	1.269
Protein residues	319	321	321	321	321	321	321
Water molecules	240	355	348	360	377	338	299
Ions	0	3	3	3	3	3	2
Ramachandran (favored/generous/disallowed)[d]	316/3/0	317/4/0	316/5/0	317/4/0	319/2/0	317/4/0	317/4/0
Ligand refinement	N/A						
Average B factor (Å^2)		49.9	35.4	31.0	24.5	57.6	70.1
Real-space correlation coefficient		0.887	0.933	0.957	0.954	0.948	0.917

[a]PDB accession ID.
[b]$R_{sym} = \Sigma| I - \langle I \rangle |/\Sigma I$, where I is the integrated intensity for a given reflection.
[c]$R_{work} = \Sigma|Fobs - Fc|/\Sigma Fobs$, where Fobs and Fc are the observed and calculated structure factor amplitudes, respectively. R_{free} is calculated as for R_{work} but from a subset of the data (5%) that was withheld from crystallographic refinement.
[d]As calculated by MolProbity (Chen et al., 2010).

level of quality as the nucleotide-free model (Experimental Procedures; Table 1). The resultant maps all showed a single region of strong, contiguous difference density inside the RPD active site that could be best fit by a single nucleoside triphosphate and three Mn^{2+} ions (Figure 2A). Anomalous difference maps confirmed the binding of manganese.

Inspection of the four NTP-bound structures revealed that the first two subdomains of the RPD form the nucleotide-binding pocket (Figure 2B). One subdomain consists of the metal-binding center of the TOPRIM fold, which coordinates all three divalent metals using a constellation of six highly conserved acidic amino acids (Figure 2C; see Figures S1 and S2A available online). The other forms an abutting ridge that is rich in invariant, basic amino acids. One of the observable Mn^{2+} ions (denoted here as metal A) is offset from the other two and makes no direct contacts with the nucleotide; by contrast, metals B and C closely associate with one side of the nucleotide triphosphate moiety, which is further sandwiched by two arginines (Arg146 and Arg221) and a lysine (Lys230) from the basic ridge. Overall, the B factors of the bound ligands (35 Å^2) are close to the average B factor for the entire protein (27 Å^2), indicating that the ligands are well ordered and bound at high occupancy (Table 1). Three of the nucleotides (CTP, GTP, and UTP) were seen to bind in a single conformation, whereas ATP adopted two orientations due to a rotation between its ribose and α-phosphate groups. An alignment of the GTP-bound structure with the *A. aeolicus*

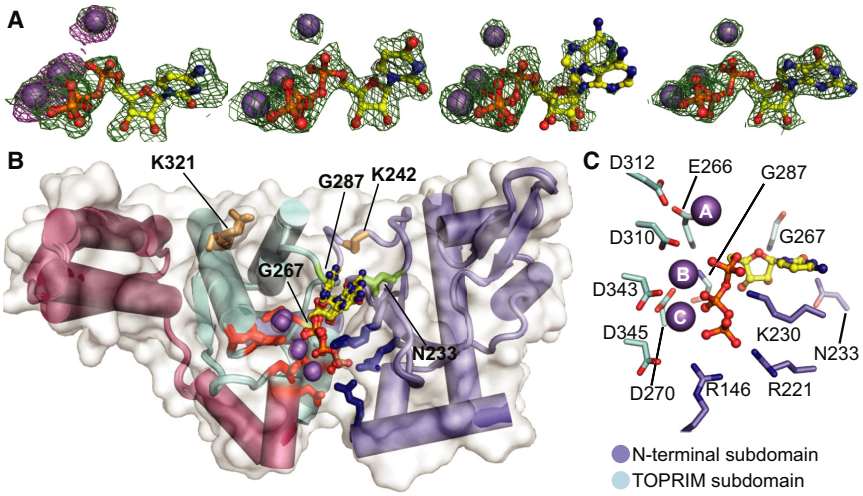

Figure 2. Overview of NTP-Bound *Sa*DnaG RPDs

(A) Difference density present in the *Sa*DnaG RPD active site for Mn^{2+}•NTP-soaked crystals is shown. From left to right, density corresponds to CTP, UTP, ATP, and GTP. The resulting difference density (mF_o-DF_c) prior to modeling of the NTP is shown contoured at 3σ as a green mesh (Experimental Procedures). Anomalous difference density maps obtained by collecting data on a CTP and Mn^{2+}-soaked crystal at the Mn-K edge are shown contoured at 5σ as purple mesh. Individual NTPs are shown from right to left as ball-and-stick representations. Mn^{2+} ions are shown as gray spheres.

(B) All four metal•NTP complexes bind to a common site on the *Sa*DnaG RPD. A superposition of the apo *Sa*DnaG RPD structure (white surface) and all four NTP-bound *Sa*DnaG RPD structures (cartoons colored by subdomain, as per Figure 1A) is shown. Side chains of metal-binding residues are shown as red sticks and side chains of basic ridge amino acids as blue sticks. NTPs and Mn^{2+} ions are shown and colored as in (A). The side chains of individual residues investigated here are labeled (*Sa*DnaG numbering), and shown as stick representations.

(C) Coordination of metal•NTP complexes. The CTP-bound structure is displayed as a representative example. NTP and Mn^{2+} ions are colored as in (A). Side chains of residues that contact the nucleotide and metal ions are labeled (*Sa*DnaG numbering), shown in stick representation, and colored according to subdomain. See also Figure S2.

or *E. coli* DnaG RPD structures reveals that the nucleotide occupies a consistently solvent-exposed region in all of the structures (Figure S2B). By varying the substituents of the soaking conditions (Experimental Procedures), we established that: (1) NTP binding is metal dependent (Figure S2C), (2) nucleotide is required for metal C to bind (Figure S2D), and (3) Mg^{2+} and Mn^{2+} are essentially interchangeable (Figure S2E).

The DnaG Nucleotide-Binding Site Is Preserved with Other TOPRIM-Dependent Enzymes

Having established that the nonproteinaceous density associated with the *Sa*DnaG RPD after soaking was a metal•NTP complex, we next asked if the nucleotide-binding configuration was adventitious, or if it reflected a pertinent mode of association consistent with primase function. One clue to resolving this question came from the relationship between DnaG and type IA/II topoisomerases. Both enzyme families employ a TOPRIM fold to promote metal-assisted catalysis of nucleotidyl phospho-transfer reactions—nucleotide addition in the case of DnaG, and reversible DNA strand scission through a catalytic tyrosine in topoisomerases (Aravind et al., 1998) (Figures 3A, 3B, and S3A). The availability of multiple topoisomerase structures, in particular a crystal structure of yeast topoisomerase II (topo II) captured as a metal-associated product complex with DNA (Schmidt et al., 2010), afforded the opportunity to compare our metal-NTP *Sa*DnaG complexes with a homologous, catalytically competent system.

To carry out this analysis, we superposed the catalytic centers of topo II and the *Sa*DnaG RPD. Only conserved C_α positions within the TOPRIM folds of the two enzymes were used in the alignments so as not to bias the relative relationship between bound substrates. Although significant variation is seen in the position and length of the outer α helices that comprise both TOPRIM folds, the three internal β strands and turns bearing the preserved catalytic acidic residues align closely (Figure 3C). The resulting comparison shows that the single catalytic metal of topo II, which engages both the reactive phosphate and the 3′ OH of the cleaved DNA strand, is coordinated by a pair of acidic amino acids (Glu449/Asp526), and that the homologous counterparts to these residues (Glu266/Asp310) ligand metal A in *Sa*DnaG. The NTP bound to the *Sa*DnaG active site also occupies the same location as the +1 nucleobase in topo II, which marks the 5′ portion of the cleaved strand resulting from DNA cleavage by this enzyme (Figure 3D). In the yeast ternary complex, the scissile phosphate associated with this nucleotide is linked covalently to the active-site tyrosine of the enzyme; superposition of the *Sa*DnaG and topo II TOPRIM folds results in a near-exact overlap of this phosphate and the α-phosphate of the bound NTP. Thus, the NTP-binding site of the *Sa*DnaG RPD maps to the same region of the TOPRIM domain that supports phosphoryl transfer in topo II and further appears to preposition the metal cofactors and reactive groups of the bound NTP in an analogous manner.

A more global inspection of the superposition between the DnaG and topo II TOPRIM folds highlights additional congruencies that reinforce the similarities between the conformation of the bound nucleotide and the incoming nucleotide seen in polymerase ternary complexes (Figure 3E). For example the orientation of the NTP in *Sa*DnaG allows for the clash-free stacking of its base against the −1 nucleobase of the DNA bound to topo II (which bears a free 3′ OH in the cleavage complex). This orientation also positions the hydrogen-bonding groups of the NTP base in-line to engage the complementary strand of the topoisomerase-bound duplex through Watson-Crick pairing (Figure 4A). Moreover, the polarity and general position of the nonscissile DNA strand paired with the TOPRIM-bound segment in topo II overlap with a previously-observed binding site for single-stranded template DNA on the DnaG RPD (Corn et al.,

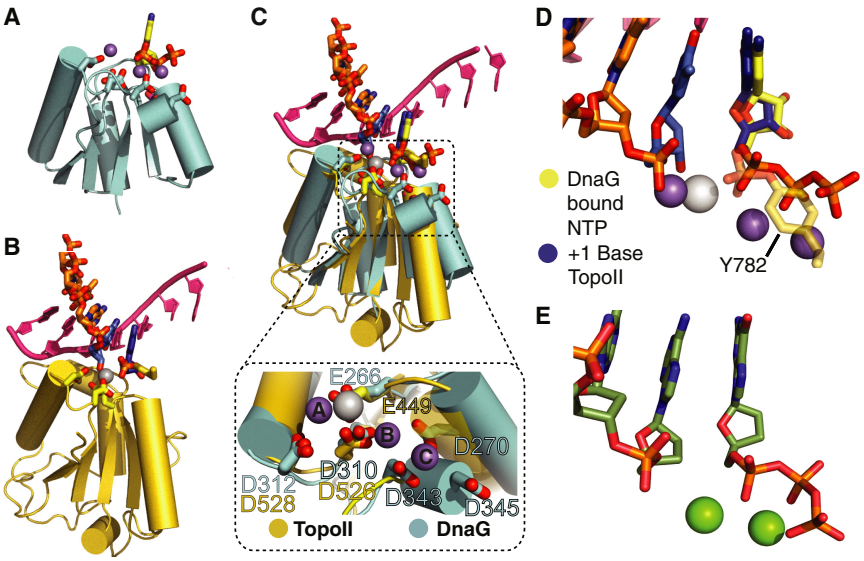

Figure 3. Alignment of Nucleotide-Bound Structures with *S. cerevisiae* Topo II

(A) Cartoon representation of the *Sa*DnaG RPD TOPRIM fold bound to nucleotide (CTP). Side chains of the conserved acidic residues in the DnaG TOPRIM fold are shown as sticks with carbon colored cyan and oxygen red. CTP and its associated Mn^{2+} ions are colored as in Figure 2A.

(B) Cartoon representation of the *S. cerevisiae* topo II TOPRIM fold as found in a DNA-cleavage complex (PDB 3L4K). Side chains of the conserved acidic residues and the covalently attached catalytic tyrosine (Tyr782) from the neighboring protomer are shown as sticks with carbon colored gold and oxygen in red. The scissile strand is shown as orange sticks. The −1 and +1 nucleobases at the cleavage site are colored blue. The complementary strand is shown in bright pink as a cartoon representation. The metal ion bound to the topo II catalytic center (Zn^{2+}, in this particular complex) is shown as a white sphere.

(C) Superposition of TOPRIM folds from CTP-bound *Sa*DnaG RPD and the yeast topo II•DNA-cleavage complex. The DnaG and topo II TOPRIM folds and side chains, along with their associated substrates, are depicted as per (A) and (B), respectively. Boxed panel is a close-up of the aligned metal-binding regions (region highlighted by dashed outline in main panel) of both TOPRIM folds, with conserved acidic residues shown as stick representations and colored as per (A) and (B). The metal ions bound to topo II and *Sa*DnaG are colored white and gray, respectively.

(D) Close-up of substrate configuration based on a TOPRIM fold alignment between DnaG and yeast topo II. Only the substrates from both structures are shown and are colored as in (C). The covalent linkage between Tyr782 and DNA observed in topo II is shown as a semitransparent stick representation.

(E) Schematic of the active site in the T7 DNA polymerase ternary complex structure (PDB 1T7P; Doublié et al., 1998) is presented. The incoming nucleotide and primer strand are shown in stick representations with carbon colored dark green. Mg^{2+} ions are shown as green spheres. See also Figure S3.

2008). Interestingly, inspection of the DNA modeled from topo II onto DnaG placed the intact DNA strand next to both an invariant lysine in subdomain I of the RPD (Lys242) and a highly conserved, basic amino acid (Lys321) in the RPD TOPRIM fold (Figure S4A). In *E. coli* DnaG the first amino acid has been shown to be important for template binding (Sun et al., 1999), whereas the latter has been shown to crosslink to the 3′ terminus of thiolated ssDNA oligonucleotides when mutated to cysteine (Corn and Berger, 2007). To determine if Lys321 also plays a role in primer synthesis by DnaG through template binding, we substituted the corresponding amino acid in *E. coli* DnaG (Arg320) with either alanine or glutamate; both mutations decreased activity in accord with the severity of the mutation (Figure 4B) and further disrupted binding to an RNA•DNA heteroduplex that mimics a preformed primer-template substrate (Figure S4B; Supplemental Experimental Procedures). Thus, the position of DNA binding to topo II, as defined by its interaction with the TOPRIM fold, provides a prospective model for considering how DnaG engages its own nucleic acid substrates.

The Nucleotide-Binding Site Is Critical for Primase Activity

Because modeling efforts such as these are by nature correlative, we next turned to mutagenesis studies to examine the manner of NTP binding. The observed NTP-binding site in *Sa*DnaG is formed by multiple highly conserved residues, many of which have been demonstrated previously to be critical for catalysis (Figures S1 and S2A; Table 2). For example the invariant acidic amino acids that ligand the metal ions involved in nucleotide coordination have been shown to be critical for metal binding and priming activity in both *E. coli* DnaG and in the related phage protein, T7 gp4 (Godson et al., 2000,; Lee and Richardson, 2005; Rodina and Godson, 2006; Urlacher and Griep, 1995). The positively charged amino acids that emerge from the basic ridge to contact the nucleotidyl triphosphate moiety likewise have been examined and found to be important for primase function (Keck et al., 2000; Rodina and Godson, 2006). In particular, substitutions at the amino acid equivalent to Lys229 in T7 gp4 (Lys128) interfere with both template-dependent and template-independent synthesis (Lee and Richardson, 2001), directly implicating this residue in nucleotide binding.

The portion of the RPD seen to surround the sugar and base of the bound nucleotide in *Sa*DnaG has received somewhat less attention. Two conserved loops in this region each bear an invariant glycine that buttresses the ribose (Gly267 and Gly287 in *Sa*DnaG) (Figure 5A). The close contacts in this interaction suggested that substitution of these amino acids with larger side chains should occlude binding of the nucleotide and abrogate primer synthesis. Mutation of the more N-terminal glycine to alanine in *E. coli* DnaG (Gly266) has been shown previously to disrupt priming activity (Rodina and Godson, 2006); using the same system, we investigated the role of the second glycine (Gly286) and found that it, too, is required for priming activity (Figure 5B). By contrast, neither glycine proved important for binding to an RNA•DNA heteroduplex (Supplemental Experimental Procedures; Figure S5), indicating that disruption of primer synthesis arises from a defect in the catalytic center. Further examination of the NTP-binding environment identified

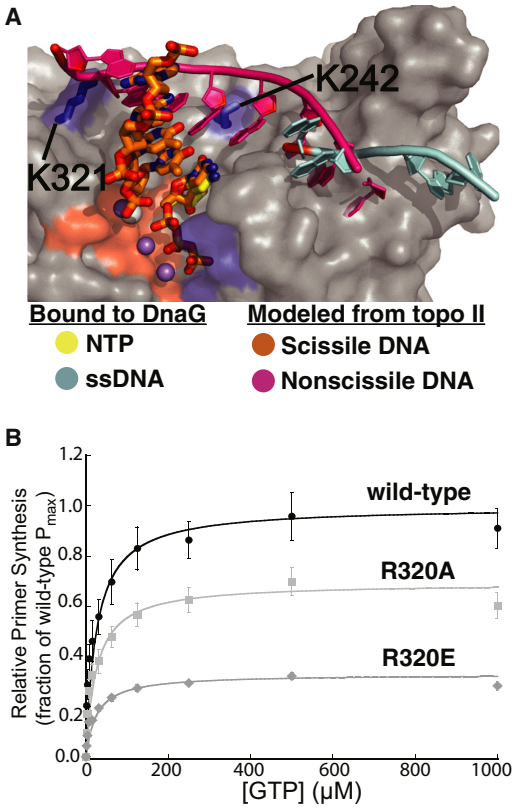

Figure 4. Congruencies between the Binding Sites for the Complementary DNA Strand in Topo II DNA and *Sa*DnaG

(A) The polarity and terminal position of the complementary DNA strand bound to the topo II TOPRIM fold line up with the site for ssDNA binding in the DnaG RPD. A superposition of the TORPIM folds between an *S. cerevisiae* topo II•DNA cleavage complex and an ssDNA-bound state of the *E. coli* DnaG RPD (PDB 3B39) is shown. The scissile strand in topo II is shown as orange sticks, and its complement as a magenta cartoon. ssDNA bound to *Ec*DnaG (cyan cartoon) is thought to mark the site of template binding (Corn and Berger, 2007; Corn et al., 2008). The protein portion of the *Sa*DnaG RPD bound to CTP (gray surface representation) is shown, with the metal-binding cluster of DnaG highlighted in red and the basic ridge in blue. The modeling implicates residues K321 and K242 of *Sa*DnaG (blue sticks with corresponding blue surfaces) as possibly playing a role in binding a primer•template product.

(B) Arg320 of *Ec*DnaG (corresponding to Lys321 in *Sa*DnaG) is required for de novo primer synthesis. Helicase-stimulated, GTP-dependent primer synthesis was assayed for the wild-type enzyme (black), Arg320Ala (light gray), and Arg320Glu (gray) mutant enzymes in a fluorometric de novo primer synthesis assay. Curves were fit as described in the Experimental Procedures, yielding the parameters listed in Table S1; error bars represent ± SEM.

See also Figure S4.

an invariant asparagine (Asn233) in subdomain I that forms a water-mediated hydrogen bond with the ribose 2′ OH (Figure 5C). As with the glycine substitutions, changing the corresponding residue in *E. coli* DnaG (Asn232) to alanine abrogated primer synthesis but had little effect on heteroduplex binding (Figure S5).

In aggregate the available biochemical data, combined with the comparative studies detailed above, strongly argue that the manner of Mn^{2+}•NTP binding to *Sa*DnaG is representative of the site and configuration used to coordinate the incoming nucleotide during strand synthesis. They also suggest that, despite their distinct active site architecture, DnaG-type primases may employ a nucleotide-addition strategy that reflects the well-established two-metal mechanism seen in other polymerases (Doublié and Ellenberger, 1998; Kiefer et al., 1998; Steitz et al., 1994). In this vein, we speculate that metal A would serve to coordinate and activate a 3′ acceptor hydroxyl for nucleophilic attack on the α-phosphate of the incoming NTP, whereas metal B would promote dissociation of the pyrophosphate-leaving group and aid metal A in transition state stabilization. Metal C, which is generally not seen in other polymerase structures, would be a distinctive feature of DnaG that could play a role in binding avidity and/or nucleotide positioning. We note that metal C is coordinated in part by two acidic amino acids (Asp343 and Asp345 in *Sa*DnaG) that are known to be important for synthesis (Godson et al., 2000) but that also comprise a unique "DPD" signature motif in DnaG family TOPRIM folds (Figure S3A) (Aravind et al., 1998; Godson et al., 2000).

Mechanism of Primase Inhibition by (p)ppGpp

The stringent response inhibits DNA replication in Gram-positive bacteria by two alarmones: pppGpp (G5P) and ppGpp (G4P) (Jain et al., 2006) (Figure 6A). Long known to block translation and transcription (Potrykus and Cashel, 2008), both nucleotides (collectively known as (p)ppGpp) have been shown recently to additionally impede primer synthesis by inhibiting DnaG through an unknown mechanism (Maciag et al., 2010; Wang et al., 2007). To understand this phenomenon, we initially attempted to model the two modified nucleotides into our NTP-bound structures; however, these efforts indicated that neither G5P nor G4P could bind to the *Sa*DnaG RPD in a manner similar to that of Mn^{2+}•NTP without introducing steric clashes between the 3′ phosphates of the alarmones and the protein.

To establish the location and orientation of G5P and G4P binding to the DnaG RPD more directly, we collected diffraction data and determined structures for crystals soaked with either G5P or G4P in the presence of divalent metal ions (Experimental Procedures). Clear difference density for both molecules (Figures 6B and 6C) revealed that the two guanosine analogs associate with the *Sa*DnaG RPD in a similar manner. Interestingly, comparison with the nucleotide-bound *Sa*DnaG complexes shows that the site of binding for G5P and G4P overlaps with the binding locus seen for the metal•NTP complexes, but only partly (Figures 6D and 6E). The 5′ phosphates and associated metal ions of both inhibitors are coordinated in an identical manner as standard nucleotides, with the exception that metal B does not appear to bind with G4P, leading its diphosphate moiety to shift over and ligand metal C. By contrast the 3′ phosphates of both alarmones directly engage metal A, an interaction that reorients the base and ribose into a configuration distinct from that seen with NTPs.

The location and arrangement of G5P and G4P in our structures suggested that the two nucleotides might impede primase activity not only by blocking entry of an incoming NTP but by also interfering with the binding of either an initiating 5′ NTP, or the extensible 3′ end of an RNA•DNA heteroduplex. To test this idea, we examined the concentration-dependent effects of both G4P and G5P on various activities of *E. coli* DnaG. As

Table 2. Conserved Residue References or Investigated in This Study

E. coli Residue	*S. aureus* Residue	T7 gp4 Residue	Putative Function	Reference
W165	S165		Template binding	Corn and Berger, 2007
R199	R200			Corn and Berger, 2007
R201	R202			Corn and Berger, 2007
K241	K242	K137		Sun et al., 1999
R320	K321			Corn and Berger, 2007; this study
E265	E266	E157	Metal A binding	Godson et al., 2000; Keck et al., 2000; Kato et al., 2003; Lee and Richardson, 2005; Rodina and Godson, 2006
D269	D270	D161	Metals B/C binding	Godson et al., 2000; Keck et al., 2000; Kato et al., 2003; Lee and Richardson, 2005; Rodina and Godson, 2006
D309	D310	D207	Metal A binding	Keck et al., 2000; Kato et al., 2003; Lee and Richardson, 2005; Rodina and Godson, 2006
D311	D312	D209	Metal B binding	Keck et al., 2000; Kato et al., 2003; Lee and Richardson, 2005; Rodina and Godson, 2006
D345	D343	D237	Metals B/C binding	Godson et al., 2000; Keck et al., 2000; Kato et al., 2003; Lee and Richardson, 2005
D347	D345	N239	Metal C binding	Godson et al., 2000; Keck et al., 2000; Kato et al., 2003; Lee and Richardson, 2005
R146	R146	R84	Basic ridge/triphosphate binding	Keck et al., 2000; Rodina and Godson, 2006
R221	R222	R124		Keck et al., 2000; Rodina and Godson, 2006
K229	K230	K128		Keck et al., 2000; Lee and Richardson, 2001; Rodina and Godson, 2006
N232	N233	K122	Nucleotide binding/incoming ribose	Lee and Richardson, 2001; Lee and Richardson, 2005; this study
G266	G267	G158		Rodina and Godson, 2006; this study
G286	G287	G181		This study

a control, we first assessed the ability of our alarmone preparations to inhibit de novo primer synthesis by full-length DnaG, using an established helicase-stimulated assay (Koepsell et al., 2005). Consistent with previously published findings by Maciag et al. (2010), we found that both nucleotides were weak inhibitors, having IC_{50} values in the low mM range (Figure 7A). We next asked if (p)ppGpp could interfere with heteroduplex binding, as might be expected if the 3′ phosphates of the inhibitors were to clash with an acceptor 3′ OH associated with metal A. Using the change in fluorescence anisotropy (FA) of a fluorescein-labeled DNA•RNA heteroduplex as a readout for binding to a primer-template substrate by the *Ec*DnaG RPD (Experimental Procedures), we observed that increasing concentrations of either G5P or G4P progressively impeded the protein from

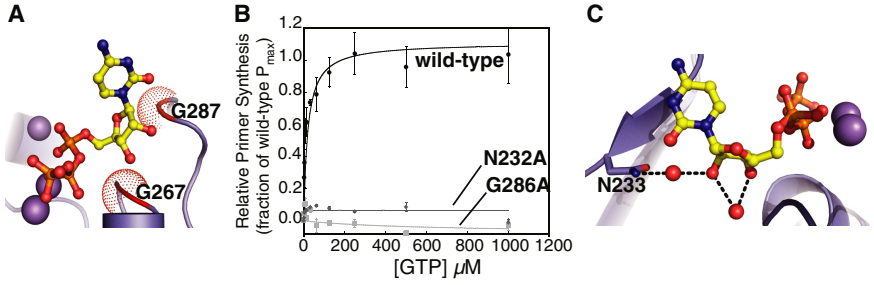

Figure 5. Analysis of Conserved Residues that Engage the Ribose of Bound Nucleotide

(A) View of the region near the ribose in the CTP-bound *Sa*DnaG RPD. The protein portion of the RPD is shown as a cartoon. Conserved residues Gly267 and Gly287 (corresponding to Gly266 and Gly286 in *Ec*DnaG) are highlighted in red, with their C_α van der Waals radii represented by red dots.

(B) Ribose-binding amino acids are critical for DnaG function. The results of a GTP-dependent, helicase-stimulated de novo primer synthesis assay are shown for wild-type (black circles), Gly286Ala (gray diamonds), and Asn232Ala (light-gray squares) *E. coli* DnaG. Curves were fit as described in the Experimental Procedures, yielding the parameters listed in Table S1; error bars represent ± SEM.

(C) Asn233 (Asn232 in *Ec*DnaG) associates with the 2′ OH of the bound nucleotide through a water-mediated hydrogen bond. Dashed lines represent hydrogen bonds.

See also Figure S5.

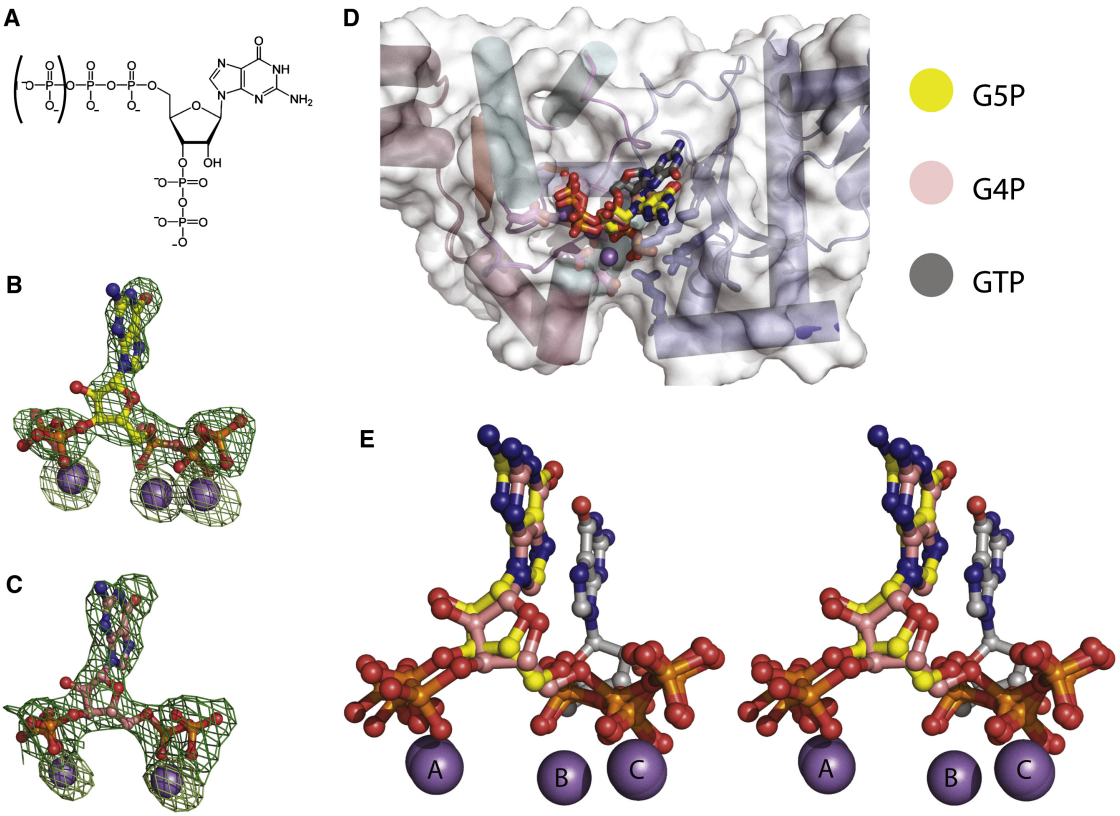

Figure 6. Binding of the *S. aureus* DnaG RPD to the Stringent Response Alarmones, pppGpp and ppGpp

(A) The chemical structure of (p)ppGpp. The phosphate enclosed in parentheses is present in pppGpp (G5P), but not ppGpp (G4P).

(B and C) Difference density present in the *Sa*DnaG RPD active site generated from crystals soaked with (B) G5P or (C) G4P. Difference density (green mesh, mF_o-DF_c) is contoured at 3σ prior to modeling of the nucleotide. Anomalous difference density generated from data collected from the same crystal at the Mn-K edge is shown as light-green mesh and is contoured at 8σ. Ball-and-stick models represent G5P (carbon in yellow) and G4P (carbon in salmon), with Mn^{2+} ions as gray spheres.

(D) Alignment of the G5P and G4P-bound structures with each other and with the GTP-bound *Sa*DnaG RPD structure. GTP is shown as a ball-and-stick model with carbon colored gray. G5P and G4P are colored as in (B) and (C), respectively. Gray spheres represent Mn^{2+} ions.

(E) Stereo image of the alignment shown in (D) (protein models omitted).

associating with the oligo (Figure 7B). Finally, we assessed the ability of (p)ppGpp to compete with GTP in a total primer synthesis assay using full-length *E. coli* DnaG. Because GTP cannot provide an initiating 3′ OH due to the start site preferences of the enzyme (5′-CTG and 5′-CAG, where the T or A position marks the 5′ terminal site of the primer), it acts as a specific probe for the accessibility of the incoming nucleotide-binding site, which both alarmones block partially in our structures (Khopde et al., 2002). This experiment revealed that G4P and G5P qualitatively exhibited mixed-type inhibitor behavior in blocking the ability of DnaG to synthesize primers in a GTP concentration-dependent manner (Figures 7C and 7D), with G5P causing a larger increase in the apparent pseudo-Michaelis-Menten constant (K_m) value (Experimental Procedures; Table S1) compared to G4P (Figures 7E and 7F). Taken together, these data are consistent with the hybrid mode of binding for (p)ppGpp observed crystallographically and indicate that, rather than acting at a distal allosteric locus, which is thought to occur during transcriptional inhibition (Srivatsan and Wang, 2008), these mediators of the stringent response take advantage of their nucleotidyl properties to directly obstruct the primase active site.

Conclusions

The mechanisms by which bacterial, DnaG-type primases synthesize primers in support of DNA replication have long remained enigmatic. By determining how bacterial primases engage nucleotide substrates, this work helps clarify one of the first steps that occurs during RNA strand polymerization. We find that NTPs bind to the active site of DnaG in an unanticipated manner that reconciles prior structural studies with biochemical work in both bacterial and phage systems and accounts for the roles of several highly conserved sequence motifs in primase function. The similarities between the active sites of DnaG and type IA/II topoisomerases, together with mutagenesis efforts, support the mode of binding we observe and implicate the NTP-binding locus as the site of nucleotide addition. Interestingly, our comparisons with topo II support earlier proposals suggesting that the newly formed heteroduplex is guided into a shallow, positively charged basin adjacent to the C-terminal

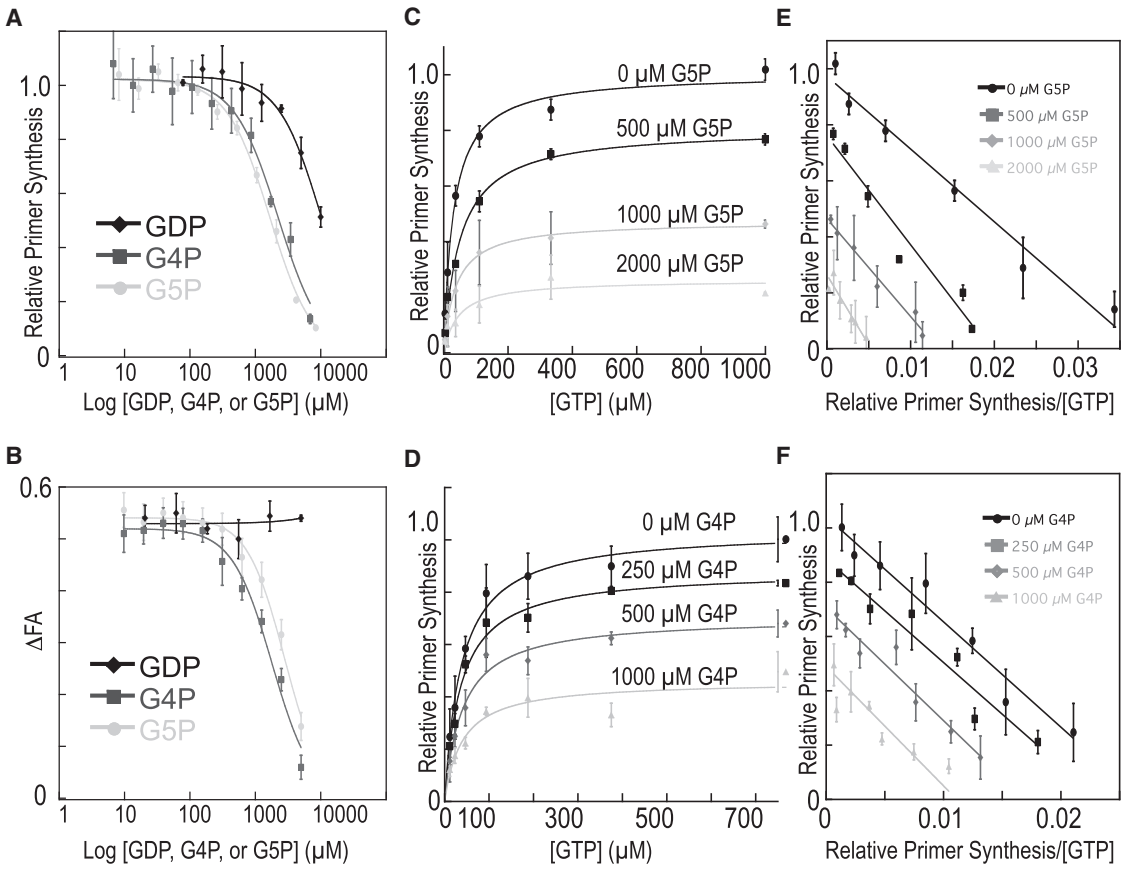

Figure 7. The Biochemical Response of the *E. coli* DnaG to G5P and G4P

(A) Concentration-dependent inhibition of *Ec*DnaG by (p)ppGpp in a helicase-stimulated de novo primer synthesis assay. G5P (light-gray circles), G4P (dark-gray squares), and GDP (black diamonds) were titrated into reactions containing full-length *E. coli* DnaG. Curves are fit to a standard IC_{50} model (Experimental Procedures); error bars represent ± SEM (Experimental Procedures).

(B) (p)ppGpp competes for product binding. Competition assays are shown for the binding of the *Ec*DnaG RPD to a fluorescently-labeled heteroduplex in the presence of increasing amounts of G5P (light-gray circles), G4P (dark-gray squares), and GDP (black diamonds). Disruption of binding was determined by measuring the change in the fluorescence anisotropy (ΔFA) of the labeled heteroduplex. Curves are fit to a standard IC_{50} model (Experimental Procedures); error bars represent ± SEM (Experimental Procedures).

(C and D) GTP-dependent inhibition of primer synthesis by G5P and G4P. GTP-dependent, helicase-stimulated de novo primer synthesis activity was measured (Experimental Procedures) against increasing concentrations of (C) G5P or (D) G4P. Points represent averages of duplicate reactions, and the range is indicated by error bars. Primer synthesis extent is reported as RPS (Experimental Procedures). Curves were fit as described in the Experimental Procedures, yielding the parameters listed in Table S1.

(E and F) GTP-dependent, helicase-stimulated primer synthesis activity from (C) and (D), respectively, treated in a manner akin to an Eadie-Hofstee plot (Eadie, 1942; Hofstee, 1952), with RPS on the y axis and RPS/[GTP] on the x axis. Linear fits to the data yield P_{max} and $K_{M,pseudo}$ values similar to those determined by nonlinear regression for (C) and (D) (Table S1).

helical subdomain as polymerization occurs (Kato et al., 2003; Keck et al., 2000; Podobnik et al., 2000) rather than past the basic ridge, which actually serves as a site for triphosphate binding. This study also reinforces recent findings showing that two small molecule alarmones produced upon induction of the stringent response, pppGpp and ppGpp, inhibit DnaG, and provides a physical explanation for the mechanism by which these agents block primase function. Future efforts, aimed at imaging higher-order ternary complexes between DnaG and distinct primer·template complexes, will be necessary to better define the chemical basis for primer initiation, elongation, and termination, as well as to more thoroughly compare the catalytic approaches employed by DnaG to those used in other polymerase systems.

EXPERIMENTAL PROCEDURES

Cloning, Expression, Purification

Ec-dnaG full-length and RPD constructs were generated previously by Keck et al. (2000). The *Sa-dnaG* RPD (residues 111–437) was cloned into a pET28b (Novagen) derivative with a tobacco etch virus (TEV) protease-cleavable, N-terminal hexahistidine tag. Mutant *E. coli* proteins were generated using QuikChange Site-Directed Mutagenesis Kit (Stratagene). The coding DNA sequence was verified for all constructs (Elim Biopharmaceuticals). All proteins were expressed in BL21 codon+ cells and purified by affinity and size exclusion chromatography. For details see Supplemental Experimental Procedures.

Crystallization of the *Sa*DnaG RPD

Final crystallization conditions for the *Sa*DnaG RPD employed a well solution of 150 mM sodium thiocyanate, 100 mM Bis-tris (pH 6.5), 13% PEG 3350, and

2% benzamidine and protein at 5 mg/ml. Crystals were soaked in well solution containing 5 mM $MnCl_2$ and 2.5 mM nucleotide, or 10 mM $MnCl_2$, 2.5 mM G4P, or G5P and 1 mM $MgCl_2$, and incubated overnight. Crystals were cryoprotected, flash frozen, and stored in liquid nitrogen prior to data collection at 100 K. For details see Supplemental Experimental Procedures.

Data Collection and Refinement

Diffraction data were collected at the Advanced Light Source Beamline 8.3.1 at Lawrence Berkeley National Laboratory (MacDowell et al., 2004). Diffraction data were indexed and integrated using XDS (Kabsch, 2010) and scaled with SCALA (Winn et al., 2011). Phases and an initial model were obtained by MR using a polyalanine model of the *E. coli* DnaG RPD (PDB 1DDE) wherein residues 115–249, residues 260–363, and residues 366–427 were each searched for separately using Phenix AutoMR (Adams et al., 2011). For soaked *Sa*DnaG RPD crystals, phases were obtained using the apo *Sa*DnaG RPD model. R_{free} flags for data collected from soaked crystals were copied from the apo data set. Refinement consisted of multiple rounds of manual rebuilding and real-space refinement with Coot (Emsley et al., 2010) and the Phenix software suite (Adams et al., 2011); real-space refinement was carried out using electron density maps calculated without the R_{free} set. NTPs and metals were not added to models until the R_{work}/R_{free} of the protein portion of the model remained stable for two rounds of refinement.

De Novo Primer Synthesis Assays

For all de novo synthesis experiments, measurements are reported here as an average of three reactions unless otherwise noted. Primer synthesis assays are based on the method described in Koepsell et al. (2005). All reactions were carried out in a total volume of 20 μl consisting of 100 mM potassium glutamate, 20 mM HEPES (pH 7.5), 0.2 mg/ml BSA, 20 mM MgOAc, and 1 mM DTT. Reactions included 0.1 mM ATP and UTP, and 500 nM full-length *Ec*DnaG and *Ec*DnaB (expressed and purified as in Corn et al., 2008). A 3′-phosphorylated, single-stranded oligonucleotide (5′-CACACACACACACA CTGAAAGCCAAAAG-3′) was used as a template DNA at 600 nM. GTP dilutions (from 4 mM to 3.9 μM) were prepared by serially diluting GTP stock (4 mM, in Tris-EDTA [TE]) 1:1 into TE. Reaction mixtures (10 μl) were incubated at room temperature (RT) for 10 min prior to addition of the GTP dilution (10 μl). Inhibitors were included in the incomplete reaction mixture. Complete reactions were incubated in a sealed 384-well plate (Bio-Rad) for 1 hr at 37°C and then stopped by addition of 10 μl of a 1:67 dilution of PicoGreen stock solution (Invitrogen) in 20 mM Tris, 50 mM EDTA (pH 7.5), giving a final stain dilution of 1:200, as per the manufacturer's instructions. Stopped reactions were incubated in the dark for 5 min, spun at 3,000 × *g* for 2 min, and raw fluorescence was measured in a PerkinElmer Victor3V multilabel plate reader. Raw fluorescence was background corrected with a no-NTP control to give fluorescence intensity (FI). The maximal amount of product produced under these conditions (P_{max}) was calculated by fitting resultant curves using nonlinear regression to a form of the Michaelis-Menten equation that accounts for the total amount of product produced by the enzyme, as opposed to the reaction rate (Equation 1). All data within a given experiment were normalized to the wild-type P_{max} (Figures 4 and 5), or the P_{max} of inhibitor-free reactions (Figure 7), and reported in terms of relative primer synthesis (RPS):

$$\mathrm{RPS} = \frac{P_{max} \times [GTP]}{K_{M,pseudo} + [GTP]}, \qquad \text{(Equation 1)}$$

where P_{max} is the maximal amount of product formed, and $K_{M,pseudo}$ is a pseudoapparent K_M that corresponds to the concentration of GTP that yields a total amount of primer synthesis equal to one-half P_{max}.

For inhibitor titrations, G5P and G4P were prepared as described by Mechold et al. (2002) and stored in desiccated form until just prior to use. Dry pellets were resuspended in 1x TE, and the concentration was measured by absorbance at 258 nm using the extinction coefficient of 13,700 $M^{-1}cm^{-1}$. GDP was prepared by dissolving GDP powder (Sigma-Aldrich) in TE to 100 mM, and the pH adjusted to 7.5. Inhibitor dilutions (7.5 μl) were prepared in TE, and mixed with an equal volume of an incomplete reaction mixture containing 2.6x Reaction Buffer, DnaG, DnaB, ATP, UTP, and template, and allowed to incubate at RT for 10 min prior to addition of GTP solution (5 μl at 400 μM). Reactions were incubated at 37°C for 1 hr, and stopped, stained, and measured using the same protocol as the standard GTP titrations. G5P was titrated from 8.4 mM to 8.2 μM, G4P was titrated from 6.9 mM to 6.8 μM, and GDP from 10 mM to 78 μM. The data were normalized to the average maximum FI to give RPS, and fit to Equation 2 (Copeland, 2005) by nonlinear regression:

$$\mathrm{RPS} = \frac{1}{1 + \left(\frac{[I]}{IC_{50}}\right)^{h}}, \qquad \text{(Equation 2)}$$

in which [I] is the inhibitor concentration, IC_{50} is the concentration of inhibitor that results in 50% inhibition, and h is the hill coefficient.

Heteroduplex Competition Assays

E. coli DnaG RPD (500 μM) was incubated with 100 nM of a 5′ fluorescein-labeled RNA•DNA heteroduplex (DNA strand [IDT] sequence: 5′-AAAAC TGCCGCCGC-3′; RNA strand [Dharmacon] sequence: 5′-GCGGCGGCA-3′) and 2x Reaction Buffer conditions at RT for 10 min. Inhibitor at 10 mM was serially diluted 1:1 into TE; dilutions were then mixed 1:1 into the 2x RPD and labeled heteroduplex mixture. All inhibitors were titrated from 5 mM to 10 μM. Reactions were incubated at RT for 30 min; fluorescent polarization (FP) was measured with a PerkinElmer Victor3V multilabel plate reader, and converted to FA prior to background correction with a no-protein control to obtain ΔFA values. The data were fit by nonlinear regression to Equation 3 (Copeland, 2005):

$$\Delta FA = \Delta FA_{min} + \frac{(\Delta FA_{max} - \Delta FA_{min})}{1 + \left(\frac{[I]}{IC_{50}}\right)^{h}}, \qquad \text{(Equation 3)}$$

in which ΔFA_{min} and ΔFA_{max} refer to the signal minimum and signal maximum, respectively, [I] is the concentration of inhibitor, IC_{50} is the concentration of inhibitor that results in 50% displacement, and h is the Hill coefficient.

Visualization and Data Analysis Methods

Structures were visualized and figures generated using PyMOL (Schrödinger, 2010). Data for activity and binding assays were processed in Microsoft Excel. Plots and corresponding fits were generated with Kaleidagraph. Sequences for sequence alignments were obtained through BLAST (Altschul et al., 1990). Alignments were calculated with MAFFT (Katoh et al., 2002), and visualized and edited with JalView (Waterhouse et al., 2009). Single-position conservation analysis was carried out in Microsoft Excel.

SUPPLEMENTAL INFORMATION

Supplemental Information includes five figures, one table, Supplemental Experimental Procedures, and Supplemental References and can be found with this article online at http://dx.doi.org/10.1016/j.str.2012.05.017.

ACKNOWLEDGMENTS

We thank Drs. Karl Drlica and Ken Dong for assistance with the manuscript, the staff at Beamline 8.3.1 for help with data collection, and the QB3 Macrolab for help generating site-directed mutants. This work was supported by the NIGMS (GM084003 to J.D.W. and GM071747 to J.M.B.) and the Welch Foundation (Grant Q-1698 to J.D.W.).

Received: April 7, 2012
Revised: May 17, 2012
Accepted: May 25, 2012
Published online: July 12, 2012

REFERENCES

Adams, P.D., Afonine, P.V., Bunkóczi, G., Chen, V.B., Echols, N., Headd, J.J., Hung, L.W., Jain, S., Kapral, G.J., Grosse Kunstleve, R.W., et al. (2011). The Phenix software for automated determination of macromolecular structures. Methods *55*, 94–106.

Altschul, S.F., Gish, W., Miller, W., Myers, E.W., and Lipman, D.J. (1990). Basic local alignment search tool. J. Mol. Biol. *215*, 403–410.

Aravind, L., Leipe, D.D., and Koonin, E.V. (1998). Toprim—a conserved catalytic domain in type IA and II topoisomerases, DnaG-type primases, OLD family nucleases and RecR proteins. Nucleic Acids Res. *26*, 4205–4213.

Bhattacharyya, S., and Griep, M.A. (2000). DnaB helicase affects the initiation specificity of *Escherichia coli* primase on single-stranded DNA templates. Biochemistry *39*, 745–752.

Carl, P.L. (1970). *Escherichia coli* mutants with temperature-sensitive synthesis of DNA. Mol. Gen. Genet. *109*, 107–122.

Chen, V.B., Arendall, W.B., 3rd, Headd, J.J., Keedy, D.A., Immormino, R.M., Kapral, G.J., Murray, L.W., Richardson, J.S., and Richardson, D.C. (2010). MolProbity: all-atom structure validation for macromolecular crystallography. Acta Crystallogr. D Biol. Crystallogr. *66*, 12–21.

Chintakayala, K., Machón, C., Haroniti, A., Larson, M.A., Hinrichs, S.H., Griep, M.A., and Soultanas, P. (2009). Allosteric regulation of the primase (DnaG) activity by the clamp-loader (tau) in vitro. Mol. Microbiol. *72*, 537–549.

Copeland, R.A. (2005). Evaluation of enzyme inhibitors in drug discovery. A guide for medicinal chemists and pharmacologists. Methods Biochem. Anal. *46*, 1–265.

Corn, J.E., and Berger, J.M. (2007). FASTDXL: a generalized screen to trap disulfide-stabilized complexes for use in structural studies. Structure *15*, 773–780.

Corn, J.E., Pease, P.J., Hura, G.L., and Berger, J.M. (2005). Crosstalk between primase subunits can act to regulate primer synthesis in trans. Mol. Cell *20*, 391–401.

Corn, J.E., Pelton, J.G., and Berger, J.M. (2008). Identification of a DNA primase template tracking site redefines the geometry of primer synthesis. Nat. Struct. Mol. Biol. *15*, 163–169.

Doublié, S., and Ellenberger, T. (1998). The mechanism of action of T7 DNA polymerase. Curr. Opin. Struct. Biol. *8*, 704–712.

Doublié, S., Tabor, S., Long, A.M., Richardson, C.C., and Ellenberger, T. (1998). Crystal structure of a bacteriophage T7 DNA replication complex at 2.2 A resolution. Nature *391*, 251–258.

Eadie, G.S. (1942). The inhibition of cholinesterase by physostigmine and prostigmine. J. Biol. Chem. *146*, 85–93.

Emsley, P., Lohkamp, B., Scott, W.G., and Cowtan, K. (2010). Features and development of Coot. Acta Crystallogr. D Biol. Crystallogr. *66*, 486–501.

Frick, D.N., and Richardson, C.C. (2001). DNA primases. Annu. Rev. Biochem. *70*, 39–80.

Godson, G.N., Schoenich, J., Sun, W., and Mustaev, A.A. (2000). Identification of the magnesium ion binding site in the catalytic center of *Escherichia coli* primase by iron cleavage. Biochemistry *39*, 332–339.

Griep, M.A., and Lokey, E.R. (1996). The role of zinc and the reactivity of cysteines in *Escherichia coli* primase. Biochemistry *35*, 8260–8267.

Hamdan, S.M., and van Oijen, A.M. (2010). Timing, coordination, and rhythm: acrobatics at the DNA replication fork. J. Biol. Chem. *285*, 18979–18983.

Heller, R.C., and Marians, K.J. (2006). Replication fork reactivation downstream of a blocked nascent leading strand. Nature *439*, 557–562.

Hofstee, B.H. (1952). On the evaluation of the constants Vm and KM in enzyme reactions. Science *116*, 329–331.

Jain, V., Kumar, M., and Chatterji, D. (2006). ppGpp: stringent response and survival. J. Microbiol. *44*, 1–10.

Kabsch, W. (2010). Xds. Acta Crystallogr. D Biol. Crystallogr. *66*, 125–132.

Kato, M., Ito, T., Wagner, G., Richardson, C.C., and Ellenberger, T. (2003). Modular architecture of the bacteriophage T7 primase couples RNA primer synthesis to DNA synthesis. Mol. Cell *11*, 1349–1360.

Katoh, K., Misawa, K., Kuma, K., and Miyata, T. (2002). MAFFT: a novel method for rapid multiple sequence alignment based on fast Fourier transform. Nucleic Acids Res. *30*, 3059–3066.

Keck, J.L., Roche, D.D., Lynch, A.S., and Berger, J.M. (2000). Structure of the RNA polymerase domain of *E. coli* primase. Science *287*, 2482–2486.

Khopde, S., Biswas, E.E., and Biswas, S.B. (2002). Affinity and sequence specificity of DNA binding and site selection for primer synthesis by *Escherichia coli* primase. Biochemistry *41*, 14820–14830.

Kiefer, J.R., Mao, C., Braman, J.C., and Beese, L.S. (1998). Visualizing DNA replication in a catalytically active *Bacillus* DNA polymerase crystal. Nature *391*, 304–307.

Kitani, T., Yoda, K.Y., Ogawa, T., and Okazaki, T. (1985). Evidence that discontinuous DNA replication in *Escherichia coli* is primed by approximately 10 to 12 residues of RNA starting with a purine. J. Mol. Biol. *184*, 45–52.

Koepsell, S.A., Hanson, S., Hinrichs, S.H., and Griep, M.A. (2005). Fluorometric assay for bacterial primases. Anal. Biochem. *339*, 353–355.

Kornberg, A.B., and Tania, A. (1992). DNA Replication, Second Edition (New York: W. H. Freeman and Company).

Kuchta, R.D., and Stengel, G. (2010). Mechanism and evolution of DNA primases. Biochim. Biophys. Acta *1804*, 1180–1189.

Lee, J.B., Hite, R.K., Hamdan, S.M., Xie, X.S., Richardson, C.C., and van Oijen, A.M. (2006). DNA primase acts as a molecular brake in DNA replication. Nature *439*, 621–624.

Lee, S.J., and Richardson, C.C. (2001). Essential lysine residues in the RNA polymerase domain of the gene 4 primase-helicase of bacteriophage T7. J. Biol. Chem. *276*, 49419–49426.

Lee, S.J., and Richardson, C.C. (2005). Acidic residues in the nucleotide-binding site of the bacteriophage T7 DNA primase. J. Biol. Chem. *280*, 26984–26991.

MacDowell, A.A., Celestre, R.S., Howells, M., McKinney, W., Krupnick, J., Cambie, D., Domning, E.E., Duarte, R.M., Kelez, N., Plate, D.W., et al. (2004). Suite of three protein crystallography beamlines with single superconducting bend magnet as the source. J. Synchrotron Radiat. *11*, 447–455.

Maciag, M., Kochanowska, M., Lyzeń, R., Wegrzyn, G., and Szalewska-Pałasz, A. (2010). ppGpp inhibits the activity of *Escherichia coli* DnaG primase. Plasmid *63*, 61–67.

Makowska-Grzyska, M., and Kaguni, J.M. (2010). Primase directs the release of DnaC from DnaB. Mol. Cell *37*, 90–101.

Marians, K.J. (1992). Prokaryotic DNA replication. Annu. Rev. Biochem. *61*, 673–719.

Mechold, U., Murphy, H., Brown, L., and Cashel, M. (2002). Intramolecular regulation of the opposing (p)ppGpp catalytic activities of Rel(Seq), the Rel/Spo enzyme from *Streptococcus equisimilis*. J. Bacteriol. *184*, 2878–2888.

Mendelman, L.V., Beauchamp, B.B., and Richardson, C.C. (1994). Requirement for a zinc motif for template recognition by the bacteriophage T7 primase. EMBO J. *13*, 3909–3916.

Mitkova, A.V., Khopde, S.M., and Biswas, S.B. (2003). Mechanism and stoichiometry of interaction of DnaG primase with DnaB helicase of *Escherichia coli* in RNA primer synthesis. J. Biol. Chem. *278*, 52253–52261.

Podobnik, M., McInerney, P., O'Donnell, M., and Kuriyan, J. (2000). A TOPRIM domain in the crystal structure of the catalytic core of *Escherichia coli* primase confirms a structural link to DNA topoisomerases. J. Mol. Biol. *300*, 353–362.

Potrykus, K., and Cashel, M. (2008). (p)ppGpp: still magical? Annu. Rev. Microbiol. *62*, 35–51.

Rodina, A., and Godson, G.N. (2006). Role of conserved amino acids in the catalytic activity of *Escherichia coli* primase. J. Bacteriol. *188*, 3614–3621.

Rowen, L., and Kornberg, A. (1978). Primase, the dnaG protein of *Escherichia coli*. An enzyme which starts DNA chains. J. Biol. Chem. *253*, 758–764.

Salzberg, S.L., Salzberg, A.J., Kerlavage, A.R., and Tomb, J.F. (1998). Skewed oligomers and origins of replication. Gene *217*, 57–67.

Schmidt, B.H., Burgin, A.B., Deweese, J.E., Osheroff, N., and Berger, J.M. (2010). A novel and unified two-metal mechanism for DNA cleavage by type II and IA topoisomerases. Nature *465*, 641–644.

Schrödinger, L. (2010). The PyMOL Molecular Graphics System, Version 1.3 Schrödinger, LLC.

Srivatsan, A., and Wang, J.D. (2008). Control of bacterial transcription, translation and replication by (p)ppGpp. Curr. Opin. Microbiol. *11*, 100–105.

Steitz, T.A., Smerdon, S.J., Jäger, J., and Joyce, C.M. (1994). A unified polymerase mechanism for nonhomologous DNA and RNA polymerases. Science *266*, 2022–2025.

Sun, W., and Godson, G.N. (1996). Interaction of *Escherichia coli* primase with a phage G4ori(c)-*E. coli* SSB complex. J. Bacteriol. *178*, 6701–6705.

Sun, W., Tormo, J., Steitz, T.A., and Godson, G.N. (1994). Domains of *Escherichia coli* primase: functional activity of a 47-kDa N-terminal proteolytic fragment. Proc. Natl. Acad. Sci. USA *91*, 11462–11466.

Sun, W., Schoneich, J., and Godson, G.N. (1999). A mutant *Escherichia coli* primase defective in elongation of primer RNA chains. J. Bacteriol. *181*, 3761–3767.

Swart, J.R., and Griep, M.A. (1995). Primer synthesis kinetics by *Escherichia coli* primase on single-stranded DNA templates. Biochemistry *34*, 16097–16106.

Tanner, N.A., Hamdan, S.M., Jergic, S., Loscha, K.V., Schaeffer, P.M., Dixon, N.E., and van Oijen, A.M. (2008). Single-molecule studies of fork dynamics in *Escherichia coli* DNA replication. Nat. Struct. Mol. Biol. *15*, 170–176.

Tougu, K., and Marians, K.J. (1996a). The extreme C terminus of primase is required for interaction with DnaB at the replication fork. J. Biol. Chem. *271*, 21391–21397.

Tougu, K., and Marians, K.J. (1996b). The interaction between helicase and primase sets the replication fork clock. J. Biol. Chem. *271*, 21398–21405.

Tougu, K., Peng, H., and Marians, K.J. (1994). Identification of a domain of *Escherichia coli* primase required for functional interaction with the DnaB helicase at the replication fork. J. Biol. Chem. *269*, 4675–4682.

Urlacher, T.M., and Griep, M.A. (1995). Magnesium acetate induces a conformational change in *Escherichia coli* primase. Biochemistry *34*, 16708–16714.

van Oijen, A.M., and Loparo, J.J. (2010). Single-molecule studies of the replisome. Annu. Rev. Biophys. *39*, 429–448.

Wang, J.D., Sanders, G.M., and Grossman, A.D. (2007). Nutritional control of elongation of DNA replication by (p)ppGpp. Cell *128*, 865–875.

Waterhouse, A.M., Procter, J.B., Martin, D.M., Clamp, M., and Barton, G.J. (2009). Jalview Version 2—a multiple sequence alignment editor and analysis workbench. Bioinformatics *25*, 1189–1191.

Winn, M.D., Ballard, C.C., Cowtan, K.D., Dodson, E.J., Emsley, P., Evans, P.R., Keegan, R.M., Krissinel, E.B., Leslie, A.G., McCoy, A., et al. (2011). Overview of the CCP4 suite and current developments. Acta Crystallogr. D Biol. Crystallogr. *67*, 235–242.

Wu, C.A., Zechner, E.L., and Marians, K.J. (1992a). Coordinated leading- and lagging-strand synthesis at the *Escherichia coli* DNA replication fork. I. Multiple effectors act to modulate Okazaki fragment size. J. Biol. Chem. *267*, 4030–4044.

Wu, C.A., Zechner, E.L., Reems, J.A., McHenry, C.S., and Marians, K.J. (1992b). Coordinated leading- and lagging-strand synthesis at the *Escherichia coli* DNA replication fork. V. Primase action regulates the cycle of Okazaki fragment synthesis. J. Biol. Chem. *267*, 4074–4083.

Zechner, E.L., Wu, C.A., and Marians, K.J. (1992). Coordinated leading- and lagging-strand synthesis at the *Escherichia coli* DNA replication fork. II. Frequency of primer synthesis and efficiency of primer utilization control Okazaki fragment size. J. Biol. Chem. *267*, 4045–4053.